



THE UNIVERSITY *of* EDINBURGH

Edinburgh Research Explorer

On the evolution of turbulent boundary layers during flame-wall interaction investigated by highly resolved laser diagnostics

Citation for published version:

Zentgraf, F, Johe, P, Nicolas, A, Barlow, R, Böhm, B, Peterson, B & Dreizler, A 2024, 'On the evolution of turbulent boundary layers during flame-wall interaction investigated by highly resolved laser diagnostics', *Combustion and Flame*, vol. 261, 113276. <https://doi.org/10.1016/j.combustflame.2023.113276>

Digital Object Identifier (DOI):

[10.1016/j.combustflame.2023.113276](https://doi.org/10.1016/j.combustflame.2023.113276)

Link:

[Link to publication record in Edinburgh Research Explorer](#)

Document Version:

Peer reviewed version

Published In:

Combustion and Flame

General rights

Copyright for the publications made accessible via the Edinburgh Research Explorer is retained by the author(s) and / or other copyright owners and it is a condition of accessing these publications that users recognise and abide by the legal requirements associated with these rights.

Take down policy

The University of Edinburgh has made every reasonable effort to ensure that Edinburgh Research Explorer content complies with UK legislation. If you believe that the public display of this file breaches copyright please contact openaccess@ed.ac.uk providing details, and we will remove access to the work immediately and investigate your claim.



On the Evolution of Turbulent Boundary Layers during Flame-Wall Interaction Investigated by Highly Resolved Laser Diagnostics

Florian Zentgraf¹, Pascal Johe¹, Alexander Nicolas², Robert S. Barlow³, Benjamin Böhm¹, Brian Peterson²,
Andreas Dreizler¹

¹ Technical University of Darmstadt, Department of Mechanical Engineering, Reactive Flows and Diagnostics, Otto-Berndt-Str. 3, 64287 Darmstadt, Germany

² University of Edinburgh, School of Engineering, Institute of Multiscale Thermofluids, Peter Guthrie Tait Road, James Clerk Maxwell Building, Edinburgh EH9 3FD, United Kingdom

³ Barlow Combustion Research, Livermore, CA, USA

Abstract

The turbulent boundary layer behavior in the presence of flame-wall interactions (FWI) has an important role on the mass and energy transfer at the gas/solid interface. Detailed experiments resolving the turbulent boundary layer evolution in the presence of FWI are lacking, which impedes knowledge. This work presents a combination of particle image velocimetry (flow field), dual-pump coherent anti-Stokes Raman spectroscopy (gas temperature), and OH laser induced fluorescence (flame topology) measurements to study the evolution of the boundary layer structure in the presence of FWI. Experiments are conducted in a side-wall quenching (SWQ) burner. Findings reveal that the reacting boundary layer flow adheres to the linear scaling law $u^+ = y^+$ in the viscous sublayer until $y^+ = 5$. Beyond $y^+ = 5$, the flame modifies the velocity and temperature field such that the u_z^+ streamwise velocity deviates from the viscous sublayer and the law-of-the-wall scaling in the log-layer with u_z^+ being smaller than that of the non-reacting flow (the subscript z refers to the streamwise coordinate and is used throughout this manuscript). As the fluid approaches the flame impingement location at the wall, the gas temperature increases significantly, causing a threefold increase in kinematic viscosity, ν . Although the near-wall streamwise velocity gradient $d\langle U_z \rangle / dy|_{y=0 \text{ mm}}$ decreases, the larger increase in ν reduces u_z^+ and leads to the deviation from the law-of-the-wall. Downstream the flame impingement location, ν is relatively constant and u_z^+ values begin to approach those of the law-of-the-wall. Trends are presented for SWQ and head-on quenching flame topologies, and are intended to help development of more accurate wall models.

This manuscript version is made available under the CC-BY-NC-ND 4.0 license <https://creativecommons.org/licenses/by-nc-nd/4.0/>.

Novelty and Significance: This work reports experimental measurements resolving the evolution of the turbulent hydrodynamic boundary in the presence of flame-wall interaction. The flame plays a significant role in modifying the turbulent boundary layer structure, as it modifies the fluid mechanics as well as the gas properties of the fluid. The energy transfer through the boundary layer is dependent on the fluid transport in the boundary layer. Experimental findings resolving the boundary layer behavior in the presence of FWI is largely absent in the literature. This work aims to fill this void, and provide useful information to the modelling community.

Author contributions: (FZ) conceptualization, methodology, investigation, data analysis, writing – original draft; (PJ) conceptualization, methodology, investigation, writing – review and editing; (AN) data analysis, writing – reviewing and editing; (RB) conceptualization, supervision, writing – review and editing; (BB) conceptualization, supervision, funding acquisition, project administration, writing – review and editing; (BP) conceptualization, supervision, funding acquisition, writing – original draft; (AD) conceptualization, supervision, funding acquisition, project administration, writing – review and editing.

Keywords: flame-wall interaction, turbulence, turbulent boundary layer, universal scaling laws

Full length article

1. Introduction

The quenching of a flame front as it interacts with a cold surface is an inherent phenomenon within most propulsion and power systems. This phenomenon, commonly referred to as flame-wall interaction (FWI), governs fuel efficiency, pollutant formation, and underpins the cooling processes required for surface durability [1,2]. As modern combustors are downsized and made to operate at higher energy densities to reach higher efficiencies and reduce carbon emissions, a larger percentage of the combustion processes will occur near surfaces for which FWI will be more significant.

During FWI, as the flame approaches the wall it interacts with the hydrodynamic boundary layer. In technically relevant environments, such as gas turbines or piston engines, a *turbulent* boundary layer exists at surfaces [3-6]. The dynamic coupling between the flame, wall, and flow modifies the mass and energy transfer at the gas/wall interface, which significantly affects the fundamental FWI behavior [7-10]. FWI in turbulent boundary layers has consequently become a prominent topic in combustion science. A significant amount of research has been dedicated to FWI in turbulent boundary layers to study the near-wall flame behavior [6,10,11], wall heat transfer [12-15], flame quenching [16-19], pollution formation and oxidation [20-23], intrinsic flame/flow interactions [5,7,9,24], and to develop more accurate numerical models for FWI simulations [25-30]. The aforementioned knowledge base has been generated from generic laboratory scale FWI environments, which have been investigated numerically using advanced numerical simulations, as well as experimentally using a range of sophisticated laser diagnostics.

A topic in FWI that has been investigated in less detail is the fundamental turbulent boundary layer development in the presence of FWI. Understanding the boundary layer structure is necessary to resolve the mass and energy transfer at the gas/wall boundary. The turbulent boundary layer structure is typically evaluated using dimensionless parameters. Thus, the ensemble mean streamwise velocity component ($\langle U \rangle$) and wall-normal distance coordinate (y) are normalized as follows [31-32]:

$$u^+ = \langle U_z \rangle / u_\tau \quad (1)$$

$$y^+ = y \cdot u_\tau / \nu \quad (2)$$

In the above equations, ν is the kinematic viscosity of the fluid at the wall and u_τ is referred to as the friction velocity:

$$u_\tau = \sqrt{\nu \left. \frac{d\langle U_z \rangle}{dy} \right|_{y=0}} \quad (3)$$

The subscript “z” used in Eqs. (1) and (3) refers to the streamwise velocity. The turbulent boundary layer is commonly delineated into different regions. The *viscous sublayer* is closest to the wall with $y^+ \leq 5$ and governed by viscous forces. The *log-layer* is farther from the wall with $y^+ > 30$ and governed by inertial forces, i.e., the turbulent Reynolds stresses. The *buffer layer* lies between the viscous sublayer and log-layer and is governed by both viscous and inertial forces. The velocity behavior in the viscous sublayer often accurately follows the relation:

$$u^+ = y^+ \quad (4)$$

There is often no defined velocity relationship in the buffer layer, while the log-layer is commonly defined by the “law-of-the-wall” model [31-32]:

$$u^+(y^+) = \frac{1}{\kappa} \ln(y^+) + B \quad (5)$$

The parameters κ and B are empirically determined constants, which most often take the value of 0.41 and 5.2, respectively. Most wall-models within computational fluid dynamic (CFD) simulations employ some form of the law-of-the-wall [1,31,32]. Wall models within CFD simulations are used to predict the mass and heat transfer at gas/solid interfaces. For turbulent flows deviating from canonical flow environments, heat transfer is often poorly predicted at surfaces. Experimental measurements are often required to tune model constants

to obtain agreement of global thermodynamic quantities between experiments and simulations. Indeed, FWI in turbulent boundary layers is a unique environment, for which the flame dynamics modifies the near-wall flow field [5,7,9,10,24,33]. As a result, the wall heat flux and the consequential FWI processes are often difficult to predict accurately and less well understood in CFD.

A thorough evaluation of the turbulent boundary layer with FWI is limited within the literature. Alshaalan and Rutland performed direct numerical simulations (DNS) of a turbulent premixed flame within a Couette channel flow assuming a simplified, single-step reaction mechanism [7]. Their flame was anchored by a flame holder, yielding a V-shaped flame where one branch of the flame interacted with the wall. This configuration is often known as a *side-wall quenching* (SWQ) configuration, where the flame propagates parallel or at an oblique angle with the wall. Alshaalan and Rutland demonstrated that u^+ velocity profiles of the reacting flow deviated significantly from those of the equivalent non-reacting flow [7]. The flame modified the streamwise velocity and shear stress at the wall, contributing to the deviation from the non-reacting flow boundary layer profile. In addition, they argued that the flame introduces additional turbulent transport mechanisms, which further modify the reacting boundary layer velocity behavior.

The DNS of Alshaalan and Rutland provide a first insight into the boundary layer behavior associated with FWI. Since that time, several DNS studies have investigated various attributes of the flame-wall-flow dynamics, but the fundamental boundary layer structure associated with FWI has been overlooked. Moreover, while DNS is a powerful tool that fully resolves the flow field and many other properties, DNS often employs simplifying assumptions (e.g., constant fluid properties, isothermal or adiabatic surfaces, single-step chemistry), which deviate from reality. It is therefore important to complement DNS and other high-fidelity simulations with experimental measurements that directly measure the flame-wall-flow dynamics. Although experiments are more limited in the spatial domain and the number of variables measured, they provide the necessary insight to understand the genuine boundary layer behavior associated with the FWI dynamics.

This work presents high-resolution particle image velocimetry (PIV) performed simultaneously with OH laser induced fluorescence (OH-LIF) to study the evolution of a turbulent boundary layer in the presence of FWI. Measurements are performed in a dedicated SWQ burner, comprised of a premixed V-flame with one flame branch impinging onto a vertical wall. To provide a reasonable measure of the fluid viscosity for proper normalization of y^+ and u^+ during FWI, complementary experiments utilizing dual-pump coherent anti-Stokes Raman spectroscopy (DP-CARS) are conducted to measure gas temperature simultaneously with OH-LIF under identical operating conditions as PIV/OH-LIF experiments. The OH-LIF in both experiments provides the means to conditionally sample the velocity field and gas temperature relative to a common flame quenching location and flame topology. This approach provides access to conditionally averaged velocity and gas temperature statistics to evaluate the inner scaling variables contributing to the large deviation of the u^+ , y^+ boundary layer structure relative to the non-reacting case. Findings are presented for both SWQ- and head-on quenching (HOQ) flame topologies, which the turbulent flame temporally alternates between in the SWQ burner [22]. Findings reveal that the flame increases velocity derived quantities at the wall primarily due to thermal expansion, but an equally large, if not larger, contributor to the change in u^+ results from the spatially variant gas temperature, which modifies the viscosity derived inner scaling quantities.

2. Experimental Approach

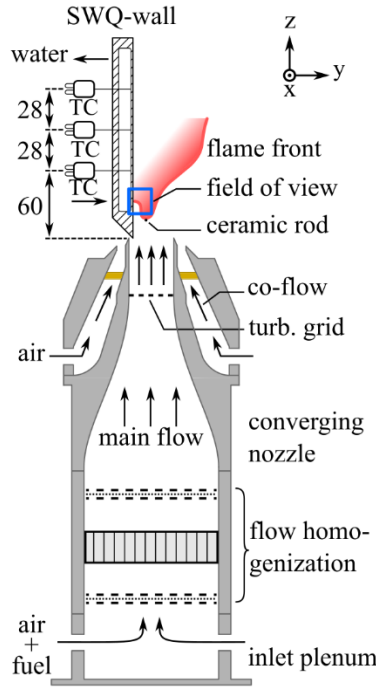
2.1. Burner Facility and Operation

Experiments were conducted in a side-wall quenching (SWQ) burner, which is shown in Fig. 1a. This burner is an established experimental facility that has been studied extensively for FWI investigations [11,20,22,24,25,34]. Details of the SWQ burner can be found in the aforementioned references, while the details relevant for this work are discussed below.

The main flow of the burner is operated with a perfectly premixed mixture of dimethyl ether (DME)-air with equivalence ratio $\Phi = 0.83$. This operation condition was selected to match the large experimental database of previous studies [11,20,22,24,25,34]. The mixture passed through a honeycomb and meshes for flow homogenization before it was guided through a converging nozzle. The flow exiting the nozzle ($40 \times 40 \text{ mm}^2$ square cross section) featured a nearly top-hat shaped streamwise velocity profile. A turbulence grid was

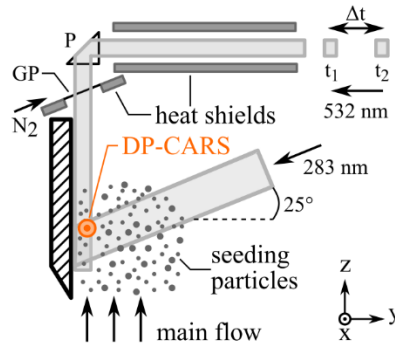
placed before the nozzle exit, which generated a turbulence intensity of $\sim 7.2\%$ in the bulk flow [34]. The Reynolds number of the main flow was 5900, based on the nozzle exit hydraulic diameter. The main flow was ignited and stabilized as a V-shaped flame on a ceramic rod with 1-mm diameter, which served as a flame holder. One branch of the V-flame impinged onto the vertical wall, where the flame locally quenched. The wall material is comprised of stainless steel and was water cooled to give a surface temperature of 330 K. A co-flow of air surrounded the main flow, and the burner was operated under atmospheric conditions.

(a) flow/burner facility

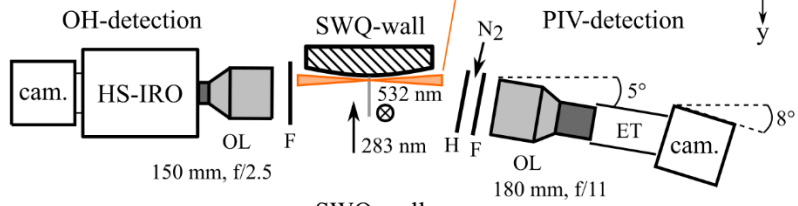


(b) laser diagnostics

excitation side (side view):



detection side (top view):



DP-CARS (front view):



TC	thermocouple
ET	extension tube
F	filter
GP	glass plate
H	heat shield
HS	high speed
IRO	intensified relay optics
OL	objective lens
P	prism

DP-CARS parts from thermochemistry setup

Fig. 1: Schematic of (a) the SWQ burner facility and (b) the applied diagnostics. Diagnostics shown in grey depict OH-LIF and PIV. Diagnostics shown in orange depict DP-CARS measurements. Numbers without units indicate dimensions in mm.

2.2 Laser Diagnostics

Two sets of experiments utilizing complementary diagnostics were performed to study the turbulent boundary layer in the presence of FWI. The first experiment consisted of high-resolution particle image velocimetry (PIV) and laser induced fluorescence of OH radicals (OH-LIF) to measure the velocity field and the flame distribution simultaneously. The second set of experiments utilized dual-pump coherent anti-Stokes Raman spectroscopy (DP-CARS) and OH-LIF to measure the gas temperature and flame distribution simultaneously. DP-CARS was additionally used to measure CO_2 alongside CO-LIF measurements for near-wall thermochemistry studies, which are reported in refs [21,22,34]. The DP-CARS and OH-LIF experiments provide a measure of the fluid viscosity, which is a function of the gas temperature, and is necessary for the calculation of the non-dimensional boundary layer variables (Eq. 1-3). The OH-LIF in both experiments provided the means to conditionally average the velocity and temperature distributions based on the flame quenching location and flame topology. This aspect enabled the use of both velocity and temperature information as a coherent dataset from the two experimental campaigns. A description of each experimental setup and data processing is provided below.

2.2.1 PIV and OH-LIF

PIV and OH-LIF were used to measure the two dimensional (2D), two component velocity field (u_y and u_z) and the 2D flame front distribution. These diagnostics were temporally synchronized and spatially matched at center plane of the wall. The lasers operated at 4 kHz repetition rate, but the detection systems operated at a 50 Hz recording rate to provide statistically independent measurements. A total of 2000 simultaneous PIV and OH-LIF images were acquired. A schematic of the combined diagnostics is shown in Fig. 1b, while a description of the setup is provided below.

For PIV, two frequency-doubled Nd:YAG lasers (Edgewave GmbH, Innoslab, IS 16II-E, 532 nm) were used to provide two laser pulses separated by $\Delta t = 10 \mu\text{s}$. The laser pulses were combined and energy controlled using half-wave plates and a polarizing beam splitter. A pair of cylindrical lenses (-30 mm and $+250 \text{ mm}$ focal lengths) and a slit aperture were used to form laser beams with homogenous intensity. A periscope was used to deflect the beams above the SWQ burner, where both pulses were formed into light sheets using a $+700 \text{ mm}$ cylindrical lens. The laser sheets were deflected downward towards the burner using a fused silica prism. The laser sheets impacted the SWQ wall at a very shallow angle to minimize reflections, while still illuminating PIV particles at the wall. The light sheets had a thickness of $\sim 250 \mu\text{m}$ ($1/e^2$ -bounds), height of 12 mm , and laser pulse energy of $225 - 390 \mu\text{J/pulse}$ within the PIV region of interest (ROI). Water-cooled heat shields protected the optics and beam path above the burner from seeding contamination, thermal damage, and beam steering. A fused silica glass plate was secured onto the heat shield and a nitrogen flow was used to mitigate thermal damage and seeding contamination [11] (see Fig. 1b).

Alumina particles (Al_2O_3 , MSE Supplies LLC, 300 nm nominal diameter) were used as PIV tracers. These particles were introduced by a customized vibrational bed seeder [34] and introduced into the air stream before the air mixed with the fuel. Mie-scattering images were recorded by a high-speed CMOS camera (Vision Research Inc., Phantom v2640) operating in double-frame mode. The camera was equipped with a 180 mm objective lens (Sigma, APO Macro DG HSM D, $f/11$) and 180 mm long extension rings for high magnification of ~ 2.25 . A bandpass filter (Edmund optics Inc., 525 nm center wavelength, 50 nm FWHM) was used to suppress flame luminosity in PIV images and a nitrogen-purged heat shield was used to reduce the thermal load from the V-flame to the lens. A Scheimpflug arrangement with respect to the x-axis (5° for objective lens, 8° for camera) minimized vignetting at the wall, while providing focused particle images [35]. The camera provided a ROI of $10.6 \text{ mm} \times 10.9 \text{ mm}$ ($\Delta y \times \Delta z$) with one camera pixel ($13.5 \mu\text{m}$) corresponding to physical dimension of $5.9 \mu\text{m}$ in the ROI.

PIV vector calculation was performed using the commercial software DaVis 10.0.5 (LaVision GmbH). Image preprocessing steps included a minimum background subtraction, a non-linear min-max filter with 9 pixels width for intensity normalization, and a 3×3 Gaussian smoothing filter. Preprocessed images were cross-correlated with decreasing window multi-pass iterations from 48×48 to 16×16 interrogation window size with 75% overlap. The PIV images had a vector spacing of $23.5 \mu\text{m}$ and spatial resolution of $94 \mu\text{m}$ depicted by the final interrogation window size. An anisotropic denoising filter was used for PIV processing. Vector post-processing was applied to exclude vectors with correlation values < 0.9 , and groups with less than 5 vectors were removed. The uncertainty in PIV measurements resulting from these high correlation values is estimated to be 3-4% based on the PIV literature [36-38]. Further details of the PIV measurements can be found in [34].

For OH-LIF, a frequency-doubled high-speed dye laser (Sirah Lasertechnik GmbH, Allegro, Rhodamine R590 dye) pumped by a frequency-doubled Nd:YAG laser (Edgewave GmbH, Innoslab, IS 8II-E) was tuned to 283.1 nm to excite the $Q_1(6)$ transition of OH. Spherical lenses (-40 mm and $+200 \text{ mm}$ focal lengths) and an aperture were used to provide a homogenous laser beam intensity. A $+500 \text{ mm}$ cylindrical lens was used to create a light sheet, which was introduced to the ROI at an inclined angle of $\approx 25^\circ$ (see Fig. 1b). In the ROI, the light sheet was $450 \mu\text{m}$ in thickness ($1/e^2$ -bounds) and 35 mm in height, with an average laser pulse energy of $250 \mu\text{J/pulse}$. The OH-LIF laser was synchronized in between the two PIV pulses.

The OH-LIF signal was acquired by a scientific high-speed CMOS camera (Photron, Fastcam SA-X2 480K, 5 μ s exposure) coupled to a high-speed image intensifier (LaVision GmbH, HS-IRO, 100 ns gate). The HS-IRO was equipped with a 150 mm UV lens (B. Halle Nachfl. GmbH, f/2.5) and bandpass interference filter (Laser Components, BP300-325). The detection system was inclined at a 10° angle with the horizontal x-axis for space considerations. The detection system provided an OH-LIF ROI of 23.1 mm x 23.6 mm (Δy x Δz) with a single camera pixel corresponding to 22.5 μ m physical distance.

OH-LIF processing was performed in MATLAB. Image preprocessing included laser beam profile correction and filtering in Fourier space to remove residual patterns of the beam profile. A 21 x 21 moving average filter was used to further suppress spatial noise. For each OH-LIF image, the local 2D gradient magnitude was calculated and the maximum gradient magnitude in the y-direction for each z-location was used to identify the flame front location. The gradient magnitude image was normalized [0 to 1] and the location where the normalized gradient on the flame front decreased below 0.15 was used to identify the quenching location [34].

2.2.2 DP-CARS and OH-LIF

The OH-LIF used in the second campaign is functionally similar to that described in Sect. 2.2.1. The major differences between the two campaigns are that the dye laser was tuned to 283.93 nm to excite the Q₁(9) transition of OH, a CCD camera (LaVision GmbH, Imager E-Lite 1.4 M) coupled to an IRO was used to record OH-LIF, and the measurements were recorded at 10 Hz. Minor differences in the optics and laser beam paths from those described in Sect. 2.2.1 also existed. These minor differences are not reported for brevity, but can be found in [21,34].

The DP-CARS setup was originally designed for near-wall thermochemistry studies in FWI environments, where the dual-pump methodology was employed to measure gas temperature and CO₂ simultaneously [21]. Only the gas temperature measurements are described here, while additional details are found in [21,34]. The relevant parts of the DP-CARS setup are colored orange in Fig. 1b. The DP-CARS approach followed that of Lucht et al. [39] to probe ro-vibrational transitions of N₂ and CO₂ molecules using three laser wavelengths λ_1 to λ_3 . Two frequency-doubled Nd:YAG lasers (Spectra-Physics PIV 400, 10 Hz, 5-8 ns pulse width) were used as pumping sources. The first Nd:YAG laser was split into two beam paths. The first beam path served as the pump at $\lambda_1 = 532$ nm. The second beam path was used to pump a custom built broad-band, modeless Stokes laser. This laser operated with a dye mixture of Rhodamine 610 and 640 resulting in a spectral profile centered around $\lambda_3 = 607$ nm with ≈ 8 nm FWHM. The second Nd:YAG laser pumped a narrow-band dye laser (Radiant Dyes Laser & Accessories GmbH, NarrowScan) operating with Rhodamine 590 dye to provide $\lambda_2 = 561.7$ nm. All three beams were energy-controlled, divergence-corrected by spherical telescopes, and included delay lines. The beams were overlapped in a planar BOXCARS arrangement and focused into the ROI using a spherical lens (+300 mm). Average pulse energies for $\lambda_1/\lambda_2/\lambda_3$ were 25/24/13 mJ in the ROI, respectively. The DP-CARS probe volume size was estimated to be (Δx , Δy , Δz) = (2.4 mm, 67 μ m, 54 μ m).

The DP-CARS signal spectrum around $\lambda_4 = 496$ nm was collected by a spherical lens (+300 mm) and separated from the spatially overlapping λ_2 radiation using three lowpass dichroic mirrors (Thorlabs Inc., DMLP550L, 90% transmission of λ_2). The λ_4 signal polarization was optimized and passed through three filters: (1) a notch filter to suppress scattering at λ_1 , (2) a shortpass filter to remove λ_2 residuals (Thorlabs Inc., FESH0550, cutoff wavelength 550 nm), and (3) optional neutral density filters to adjust the temperature-dependent DP-CARS signal intensity between fresh gas and burned gas regions. The signal was focused into a 1-m spectrometer (SPEX Industries Inc., 1704, 2400 lines/mm grating) by a +100 mm spherical lens and recorded by a cooled, backside-illuminated CCD camera (Princeton Instruments, Pixis 400, 1 ms exposure). Non-resonant DP-CARS spectra were recorded in pure argon gas to correct for the profile of the Stokes laser.

A spectral fitting algorithm [40] was used to process gas temperature from the DP-CARS spectra. The raw spectra were corrected by a mean background subtraction and normalized by the non-resonant background. The square root of the corrected spectra was taken, and a dispersion calibration was used to designate wavenumbers of the spectrum. This procedure was applied to single-shot spectra, providing single-shot gas temperature measurements. The accuracy and precision of the DP-CARS temperature is assessed using the

unbounded branch of the V-flame as an adiabatic reference case as detailed in [21,34]. A conservative estimate of the accuracy is reported as 3%, while the precision is reported as 4%. Further details of the DP-CARS processing are described in [21,22,34].

The objective of DP-CARS was to measure gas temperatures at fixed wall-normal distances as well as various z -locations relative to the flame quenching height. To meet this objective, the DP-CARS probe volume was positioned at a single z -location ($z = 48$ mm above the nozzle exit) where FWI occurred on average. The DP-CARS probe volume was placed at $y = 120$ μm from the wall. Measurements were performed at discrete wall normal locations by translating the SWQ burner in increments of 100 μm from $y = 120$ μm to $y = 1$ mm; additional measurements were performed at $y = 1.5$ mm, 2 mm, and 4 mm. At y -locations less than 1.5 mm, 7500 DP-CARS measurements were recorded, while at y -locations greater than 1.5 mm, 1000 DP-CARS measurements were recorded alongside OH-LIF. As documented in Zentgraf et al. [22], the turbulent flow creates a quasi-periodically flapping motion of the flame. This flapping motion provided a range of flame quenching heights relative to the probe volume at its fixed z -location. Thus, it was not necessary to perform DP-CARS measurements at several z -locations.

3. Flame topology

As mentioned, the turbulent flame operation in the SWQ-burner exhibits a quasi-periodic flapping motion, where the flame transitions between a *HOQ-like* and *SWQ-like* configuration [22]. Figure 2 shows examples of these flame topologies within individual OH-LIF images. A SWQ topology exists when the flame impacts the wall at a shallow angle and the flame propagates nearly parallel to the surface. The HOQ topology exists when a significant portion of the flame is parallel to the wall and propagates normal to the surface. Zentgraf et al. demonstrated that under turbulent operation in the SWQ burner, the flame alternates between HOQ and SWQ on the order of 5 ms or less [22]. With a recording rate of 50 Hz and 10 Hz, it was ensured that several quenching events would occur between successive measurements to provide statistically independent measurements.

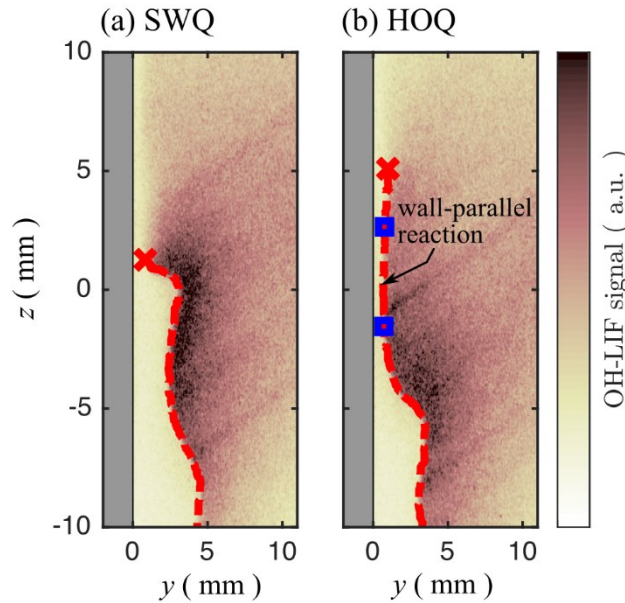


Fig. 2: Individual OH-LIF images depicting SWQ and HOQ flame topologies. Red crosses indicate the farthest downstream flame location identified as the quenching location. Blue squares indicate the location of the wall-parallel flame section in HOQ topologies.

The flame topology at the wall is anticipated to influence the turbulent boundary layer development. Therefore, in this work the turbulent boundary layer analyses are conditioned in relation to SWQ and HOQ topologies. To classify the flame topology for each instantaneous measurement, the quenching point was first identified as described in Sect. 2.2.1. Subsequently, the flame front was analyzed upstream of the quenching point to distinguish between SWQ and HOQ topologies. If flame locations upstream the quenching point are farther

away from the wall than the quenching point, then the flame topology is classified as SWQ. In contrast, if flame locations are closer to the wall than the farthest downstream quenching point and exhibited a flame section parallel to the wall, the flame topology is identified as HOQ. Within the experiments performed in this work, approximately 43.4% of the flame topologies in the OH-LIF images were classified as SWQ (868 samples) and 56.6% were identified as HOQ (1132 samples).

All measurements in this work were categorized as either SWQ or HOQ. The measurements were then conditioned relative to the flame quenching height for SWQ cases (red cross in Fig. 2a), and the farthest upstream wall-parallel flame location for HOQ cases (lower blue square in Fig. 2b). This procedure provided the means to analyze velocity and temperature statistics relative to important flame features in the SWQ and HOQ cases, and is adopted throughout the reacting flow datasets presented in this work.

4. Results and Discussion

4.1 Non-Reacting Reference Case

Velocimetry measurements of the non-reacting boundary layer flow within the SWQ flow facility are used as a reference case to benchmark the boundary layer measurements performed under reacting conditions. For the non-reacting flow operation, the SWQ burner operated with the same fuel/air flow rates through the burner. The ensemble average non-reacting velocity field is shown in Fig. 3a. The center of the field-of-view (FOV) is located $z = 48$ mm above the nozzle exit, where FWI occurs under reacting flow conditions. The z -locations shown in Fig. 3a are relative to the $z = 48$ mm location. The wall-normal boundary layer profile, normalized by the inner variable to yield u_z^+ , y^+ components, is shown in Fig. 3b. In this work, the subscript “ z ” is used to indicate the z (streamwise) direction. This velocity profile is extracted from the ensemble averaged velocity field and is spatially averaged over a $z = 0 \pm 130$ μm location (see Fig. 3a) comprising of 11 vectors in the z -direction. The variable y^+ , shown in Fig. 3b, is calculated at ambient conditions (1 bar and 20°C; $\nu = 1.516 \times 10^{-5}$ m²/s) from [41].

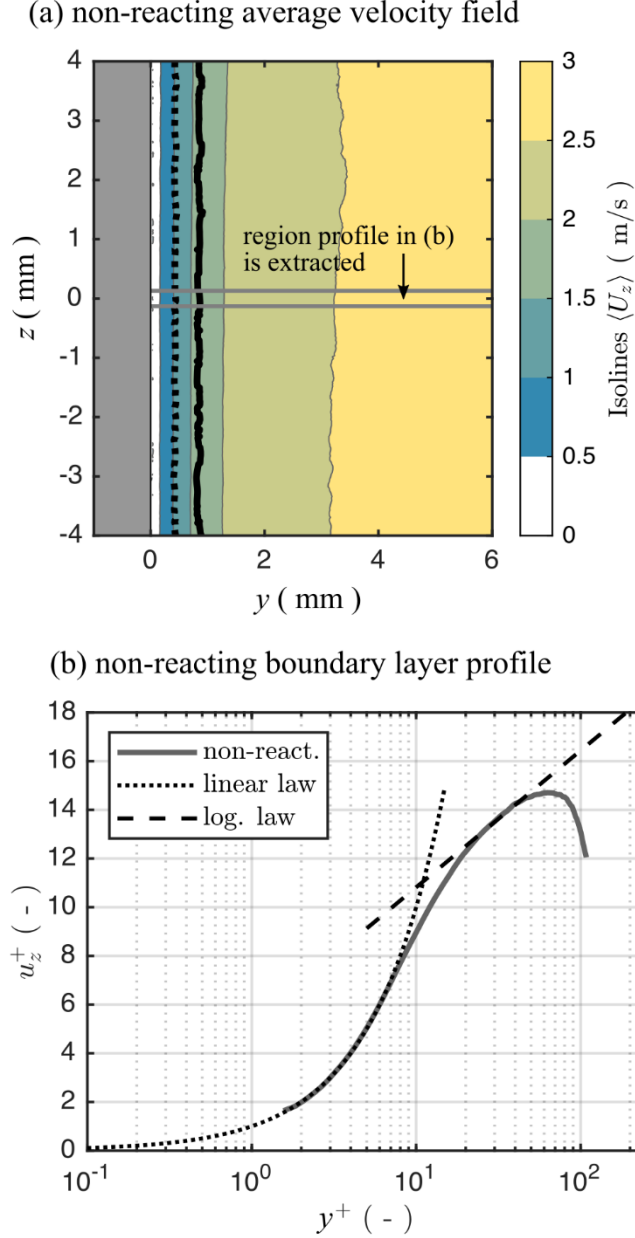


Fig. 3: Non-reacting reference case. (a) 2D streamwise velocity $\langle U_z \rangle$ with the physical streamwise locations of $y^+ = 5$ (dotted black line) and $y^+ = 10$ (solid black line) shown. (b) u_z^+, y^+ profile spatially averaged over a $z = 0 \pm 130 \mu\text{m}$ region (see gray horizontal lines in (a)). Statistics are composed from 300 PIV images.

The u_z^+ profile shown in Fig. 3b shows strong agreement within the linear-law in the viscous sublayer ($u_z^+ = y^+$). For these high-resolution PIV measurements, approximately 20 data points exist within the viscous sublayer ($y^+ \leq 5$). The u_z^+ profile also shows good agreement within the log-layer, for which the long-dashed line in the log-layer is represented by Eq. 5. At $y^+ = 60$, which is approximately $y = 5.6$ mm, the u_z^+ profile begins to deviate from the log-law due to the wake region of the ceramic rod acting as a flame holder in the SWQ burner. The core of the wake region is located at $y = 9 - 10$ mm.

The physical locations of $y^+ = 5$ and 10 are shown along the streamwise distance as dotted and solid black lines within the velocity field in Fig. 3a. The physical locations of these y^+ values are constant in the streamwise direction with $y^+ = 5$ corresponding to $y = 465 \mu\text{m}$ and $y^+ = 10$ corresponding to $y = 935 \mu\text{m}$. The constant location of the y^+ values indicate that the turbulent boundary layer is not growing significantly within the 8 mm streamwise distance at this z -location (48 mm above the nozzle exit) under the turbulent conditions employed. Further details of the non-reacting boundary layer in the SWQ facility are described in [34,42].

4.2 Reacting boundary layer

4.2.1 Ensemble-average stream-wise flow field

Figure 4 shows the $\langle U_z \rangle$ flow fields conditioned by the SWQ and HOQ flame topologies. The $z = 0$ mm position represents the quenching location for SWQ cases, while $z = 0$ mm represents the farthest upstream wall-parallel flame front location for the HOQ cases. Similar to Fig. 3a, the $y^+ = 5$ and 10 isolines are shown as a function of streamwise distance. The red dashed line represents the ensemble averaged flame location when flame contours are conditionally averaged at the $z = 0$ mm location. This represents the flame brush centroid in the y -direction for each z -location. 2D temperature and viscosity fields are also shown in Fig. 4. The average temperature field is derived from DP-CARS measurements. The single-shot temperature data was interpolated onto a grid that corresponded to the PIV grid. The kinematic viscosity field is calculated from gas temperature field using tabulated air viscosity values reported in [41].

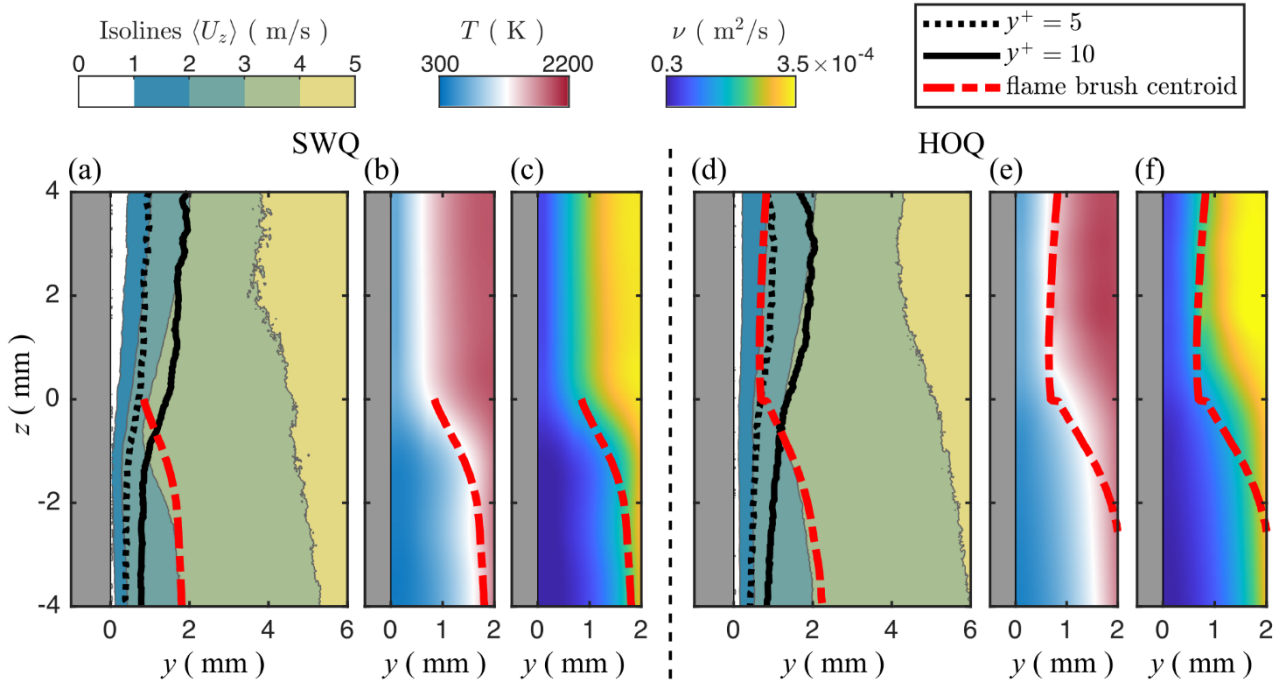


Fig. 4: (a,d) Streamwise $\langle U_z \rangle$ velocity, (b,e) temperature, and (c,f) viscosity fields associated with SWQ and HOQ cases. Black dotted lines and black solid lines depict physical locations of $y^+ = 5$ and $y^+ = 10$, respectively. Red dashed line depicts flame brush centroid.

The $\langle U_z \rangle$ flow fields presented in Fig. 4 exhibit appreciable differences from the non-reacting boundary layer flow field shown in Fig. 3a. In particular, $\langle U_z \rangle$ velocity magnitudes are appreciably higher for the reacting boundary layer flow field shown in Fig. 4. Higher velocities are a result of gas expansion across the flame front, which accelerates the fluid and, in the process, entrains fresh gas into the flame. As the flame approaches the wall, the flame imparts higher $\langle U_z \rangle$ velocity magnitudes closer to the wall particularly in the region from $-2 \leq z \leq 0$ mm. For SWQ cases, $\langle U_z \rangle$ as large as 3 m/s are imposed as close as $y = 820$ μ m, which is inside the $y^+ = 10$ isoline. The mean flame brush location for SWQ cases also penetrates past $y^+ = 10$, but stops at $y = 840$ μ m, which is just short of the viscous sublayer at $y^+ = 5$. For the HOQ case, $\langle U_z \rangle$ in excess of 3 m/s do not penetrate as close to the wall as in the SWQ case. However, for the HOQ case, the mean flame brush location is shown to penetrate within $y^+ = 5$ and reaches as close as $y = 650$ μ m from the wall. As described in the literature [2,16,43], the quenching distance is lower for HOQ flames, which is argued to be the reason why HOQ cases penetrate farther into the viscous sublayer than SWQ cases. For comparison, the non-reacting boundary layer flow exhibits $\langle U_z \rangle$ velocity magnitudes up to 1.5 m/s at $y^+ = 10$, which is approximately half the velocity magnitude of the reacting flow at this location.

Downstream of the $z = 0$ mm location, the fluid at the wall expands due to an increase in temperature. Consequently, a burned gas boundary layer develops downstream from $z = 0$ mm in both the SWQ and HOQ cases. This burned gas boundary layer is similar to that qualitatively described by Jainski et al. [24]. In the

burned gas layer, lower $\langle U_z \rangle$ velocity magnitudes extend outwards from the wall. The $y^+ = 5$ and 10 isolines are shown to extend farther away from the wall and into higher $\langle U_z \rangle$ velocity magnitudes in the burned gas boundary layer. These features suggest a mildly growing burned gas boundary layer above $z = 0$ mm.

4.2.2 Evaluation of inner scaling parameters

In this work, the non-dimensional boundary layer variables u_z^+, y^+ are computed to evaluate the reacting turbulent boundary layer structure. Before evaluating the non-dimensional variables, it is important to understand how individual variables embedded within u_z^+, y^+ are affected by the quenching flame. Therefore, Fig. 5 evaluates the streamwise quantities of (a) mean gas-phase temperature, (b) mean kinematic viscosity, ν , (c) mean streamwise velocity $\langle U_z \rangle$ at $y = 120 \mu\text{m}$, (d) mean velocity gradient $d\langle U_z \rangle/dy$, and (e) friction velocity $u_{\tau,z}$ for the SWQ flame topology at selected y -locations. Figure 5f shows the 2D streamwise velocity field $\langle U_z \rangle$, including the $y^+ = 5, 10$ isolines and the mean flame location as shown in Fig. 4.

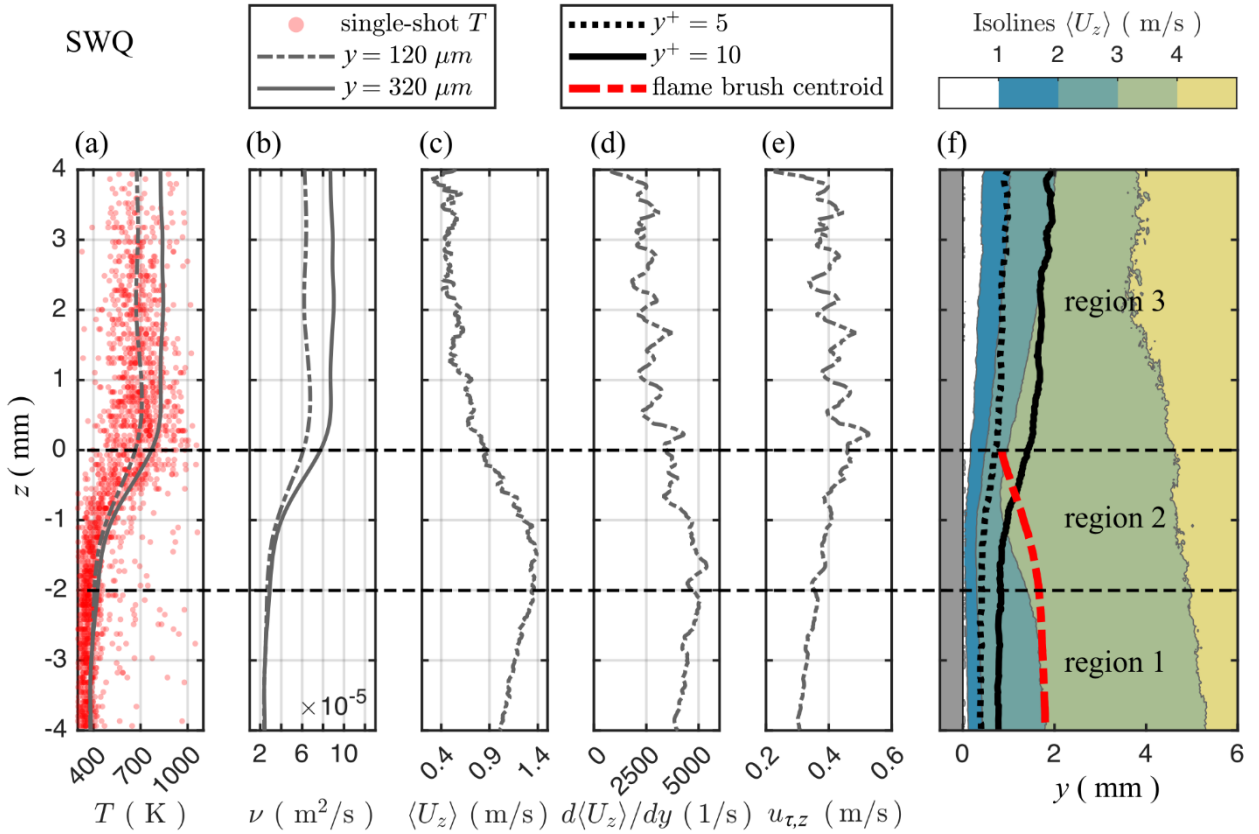


Fig. 5: Streamwise values of key parameters associated with non-dimensional boundary layer variables u_z^+, y^+ for SWQ cases. Statistical information: 2655 samples for temperature-related quantities (a,b) and 868 samples for velocity-related quantities (c-f).

The temperature and viscosity profiles in Fig. 5a,b are shown at selected physical distances from the wall. The location of $y = 120 \mu\text{m}$ denotes the DP-CARS measurement location closest to the wall. Measurements at $y = 120 \mu\text{m}$ are used to determine viscosity to calculate y^+ and $u_{\tau,z}$ (see Eq. 2 and 3). The red data points shown in Fig. 5a are individual DP-CARS temperature measurements at $y = 120 \mu\text{m}$. The scatter in the data is low for $z \leq 1$ mm, but increases near the quenching height and farther downstream. The large scatter beyond $z > 1$ mm can occur due to (1) variances in the quenching distance (Δy), (2) thermal mixing between hot products / fresh gas in each individual measurement, or (3) beam steering in the DP-CARS measurements. Thermal mixing is expected downstream of the quenching height, but it has also been reported that hot products can be transported into the fresh gas ahead of the quenching height [22,23], which would induce the scatter below $z = 0$ mm. The temperature and viscosity profiles shown at $y = 320 \mu\text{m}$ wall distance are given to inform the reader of how quickly gas temperature changes spatially within the reacting near-wall environment. It should be emphasized that the boundary of the viscous sublayer at $y^+ = 5$ is no less than $y = 465 \mu\text{m}$ within the FOV.

Thus, values reported for the $y = 120 \mu\text{m}$ and $320 \mu\text{m}$ locations fall within the viscous sublayer region of the boundary layer.

The near-wall velocity behaves linearly in the viscous sublayer, such that its velocity gradient is constant:

$$d\langle U_z \rangle / dy|_{y^+ < 5} = \text{constant} \quad (6)$$

The streamwise velocity gradient was approximated by applying a linear fit to the velocity values within the viscous sublayer at each streamwise location, which is explained in further detail in [34]. The local $d\langle U_z \rangle / dy$ value is used to calculate $u_{\tau,z}$ as a function of streamwise distance.

The profiles shown in Fig. 5 are evaluated in three regions relative to the quenching height. The first region (region 1) refers to streamwise locations from $-4 \leq z \leq -2 \text{ mm}$, where the flame is relatively parallel to the wall and far enough away from the wall that the gas temperature and viscosity are less affected by the flame and are relatively constant. The streamwise velocity closest to the wall increases linearly from $-4 \leq z \leq -2 \text{ mm}$, reaching a near maximum of 1.4 m/s at $z = -2 \text{ mm}$ as shown in Fig. 5c. The increase in $\langle U_z \rangle$ occurs as the flame approaches the wall and increases the velocity of the unburned gas between the flame and wall. The streamwise velocity gradient at the wall shows an equally steady increase as a result of $\langle U_z \rangle$ increasing. As a result, $u_{\tau,z}$ exhibits a linear increase within the unburned region from $-4 \leq z \leq -2 \text{ mm}$.

The second region (region 2) corresponds to $-2 \leq z \leq 0 \text{ mm}$, where the flame brush approaches the wall, leading to a substantial increase in gas temperature. As a result, ν increases from 2×10^{-5} to $6 \times 10^{-5} \text{ m}^2/\text{s}$ at the $y = 120 \mu\text{m}$ location. As the flame approaches the wall, $\langle U_z \rangle$ reaches a maximum value of 1.4 m/s , which persists until $z \sim -1 \text{ mm}$. From $-1 \leq z \leq 0 \text{ mm}$, $\langle U_z \rangle$ at $y = 120 \mu\text{m}$ decreases significantly to 0.8 m/s , which is lower than the initial $\langle U_z \rangle$ velocity of 1.0 m/s at $z = -4 \text{ mm}$. The decrease in $\langle U_z \rangle$ is likely due to the increase in ν of the unburned gas. The trend of $d\langle U_z \rangle / dy$ at the wall mimics that of $\langle U_z \rangle$. The trend of $u_{\tau,z}$ results from the competing effects between ν and $d\langle U_z \rangle / dy$. Figure 5e shows that $u_{\tau,z}$ continues to increase linearly by approximately 30% in region 2 as the fluid approaches the quenching location. This increase is a direct result of kinematic viscosity increasing more substantially than the decrease in $d\langle U_z \rangle / dy$ (ν increases by 300%, while $d\langle U_z \rangle / dy$ decreases by $\sim 25\%$).

The final region (region 3) corresponds to the region directly downstream of the quenching location from $0 < z \leq 4 \text{ mm}$, where a burned gas boundary layer develops. Downstream $z = 0 \text{ mm}$, Figs. 5a,b show that gas temperature and viscosity stabilize and are approximately constant in region 3. The $\langle U_z \rangle$ velocity at $y = 120 \mu\text{m}$ are shown to decrease steadily by 55% in the streamwise direction in region 3. The lower $\langle U_z \rangle$ velocities in region 3 is attributed to the increased viscosity within the viscous sublayer as well as thermal expansion of the sublayer fluid, which shifts streamlines away from the wall. The decreasing trend of $d\langle U_z \rangle / dy$ in Fig. 5d emulates that of $\langle U_z \rangle$ in region 3. Larger fluctuations in $d\langle U_z \rangle / dy$ occur due to lower signal-to-noise levels at the wall in burned gas regions. Values of $u_{\tau,z}$ in region 3 are shown to decrease due to near constant values of ν and decreasing $d\langle U_z \rangle / dy$ values. $u_{\tau,z}$ values exhibit similar fluctuations as shown for $d\langle U_z \rangle / dy$ due to the lower signal quality at the wall in the burned gas.

The profiles shown in Fig. 5a-e also describe the evolution of y^+ as a function of streamwise distance. Although both ν and $u_{\tau,z}$ vary as a function of z , the changes in viscosity are far greater than that of friction velocity. As such, the streamwise trend of y^+ adheres more to the streamwise increase in ν due to the increase in temperature. The aforementioned trends demonstrate that the reacting turbulent boundary layer environment has additional complexity over the non-reacting turbulent boundary layers, with gas temperature having a significant role in the boundary layer fluid mechanics.

Figure 6 evaluates the same inner scaling parameters as a function of streamwise location, but now for HOQ flame topologies. With regards to streamwise quantities, one of the leading differences between HOQ and SWQ topologies is that HOQ has significantly greater variability in the measured near-wall gas temperature as depicted by the scatter in the datapoints shown in Fig. 6a. The larger scatter in gas temperature measurements is due to the strong variability of the local flame location relative to the wall. This aspect is more severe for HOQ than for SWQ flame topologies. For the HOQ flame topologies, the formation of the wall-parallel flame section can exist as far as 1 mm from the wall as the flame first approaches the wall, or as close as $350 \mu\text{m}$ from the wall when the HOQ flame quenches. With a measurement location of $y = 120 \mu\text{m}$, the measurement

can either sample gas far from or close to the flame, which explains the large temperature variation above $z = -1$ mm in Fig. 6a. The high temperature in excess of 600 K shown below $z < -1$ mm occurs when the HOQ flame exhibits mild curvature, for which the flame upstream the wall-parallel flame location is in close proximity to the wall, sometimes only 100 μm further away from the wall than the wall-parallel flame segment.

The larger temperature scatter for HOQ cases creates a weaker perceived temperature gradient in the ensemble-average temperature profile shown in Fig. 6a. The average gas temperature increases mildly from $-4 \leq z \leq -1$ mm and then shows a sharper increase in temperature from $-1 < z \leq 1$ mm. Downstream $z > 1$ mm, the temperature profile plateaus to a temperature similar to the SWQ topology. The average viscosity profile emulates that of the average temperature profile. Although ν increases by nearly the same amount over the $-4 \leq z \leq 4$ mm distance for the HOQ and SWQ cases, the increase in ν occurs over a larger distance for HOQ. For example, at $y = 120 \mu\text{m}$ ν increases from 2×10^{-5} to $3.5 \times 10^{-5} \text{ m}^2/\text{s}$ in region 1 ($-4 \leq z \leq 2$ mm), and increases to $5.5 \times 10^{-5} \text{ m}^2/\text{s}$ in region 2 ($-2 \leq z \leq 0$ mm) for HOQ. This is in sharp contrast to SWQ, where an increase in ν from 2×10^{-5} to $6 \times 10^{-5} \text{ m}^2/\text{s}$ at $y = 120 \mu\text{m}$ solely occurs in region 2. At $y = 120 \mu\text{m}$, the maximum ν of $7.2 \times 10^{-5} \text{ m}^2/\text{s}$ is reached in region 3 ($0 < z \leq 4$ mm) and is comparable for HOQ and SWQ.

Variation in the HOQ flame front location is primarily responsible for the larger temperature scatter and the weaker perceived mean temperature and viscosity gradients in Figs. 6a,b. Spatially-resolved, single-shot temperature measurements as demonstrated in [13,44,45], in addition to more selective conditional averaging could better resolve spatial gradients with less variation. However, this is beyond the scope of this work. The scatter in temperature effectively makes it more difficult to provide an accurate representation of the average ν profile for HOQ cases. The large gas temperature variations will undoubtedly affect the fluid mechanics at the wall (e.g., $\langle U_z \rangle$ and $d\langle U_z \rangle / dy$). Thus, it is expected that the $\langle U_z \rangle$ and $d\langle U_z \rangle / dy$ profiles reported in Fig. 6c,d will exhibit an average behavior between the temperatures shown in the scatter. As such, the calculation of inner variables for HOQ as a function of streamwise distance should be taken with caution. Nonetheless, this work presents a first attempt to describe the reacting turbulent boundary layer in FWI environments from experiments, as well as distinguish the boundary layer behavior between SWQ and HOQ flame topologies.

The velocity related profiles in Fig. 6 are evaluated in the aforementioned regions 1-3. However, since the trends in regions 1 and 2 are similar, findings for regions 1 and 2 are combined into the same discussion.

In regions 1 and 2 ($-4 \leq z \leq 0$ mm), Fig. 6c shows that the near-wall streamwise velocity $\langle U_z \rangle$ at $y = 120 \mu\text{m}$ exhibits a mild increase from $\approx 0.85 \text{ m/s}$ to $\approx 1 \text{ m/s}$. The increase in $\langle U_z \rangle$ and its overall magnitude are lower for HOQ than SWQ cases. As shown in Fig. 5f for SWQ, higher velocities near the flame impinge closer to the wall, which is not present for the HOQ case (Fig. 6f). $d\langle U_z \rangle / dy$ values in Fig. 6d exhibit a rather constant profile from $-4 \leq z \leq 0$ mm. The $u_{\tau,z}$ profile in Fig. 6e shows an appreciable linear increase from 0.3 m/s to 0.45 m/s, which is consistent with the SWQ findings. Since $d\langle U_z \rangle / dy$ is approximately constant from $-4 \leq z \leq 0$ mm, the increase in ν appears to be the primary reason for the increase in $u_{\tau,z}$ in regions 1 and 2 for HOQ.

Downstream $z = 0$ mm in region 3, gas temperatures show a mild increase and then plateau near $z = 1$ mm in Fig. 6a. Although the flame is not yet quenched for the HOQ case, the $\langle U_z \rangle$ velocity at the wall exhibits the same decreasing trend above $z = 0$ mm (Fig. 6c). Similar to SWQ, the lower velocities may be due to a more viscous fluid at the wall and due to slower thermal expansion in the burned gas boundary layer. In Fig. 6d, $d\langle U_z \rangle / dy$ exhibits a mild decrease above $z = 0$ mm, while $u_{\tau,z}$ features relatively constant values between 0.45-0.50 m/s (Fig. 6e).

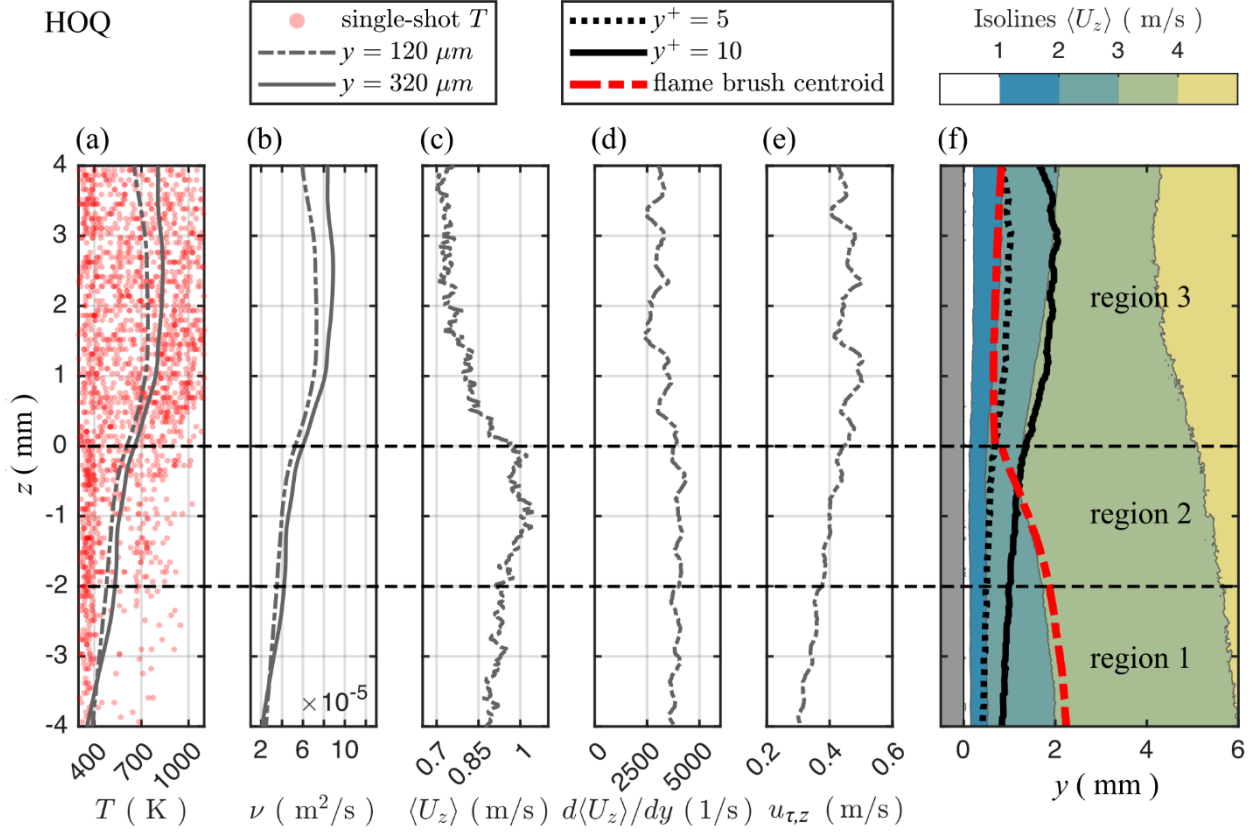


Fig. 6: Streamwise values of key parameters associated with non-dimensional boundary layer variables u_z^+, y^+ for HOQ cases. Statistical information: 2632 samples for temperature-related quantities (a,b) and 1132 samples for velocity-related quantities (c-f).

In Fig. 6f, the location of $y^+ = 5$ and 10 values as a function of streamwise distance exhibit a similar trend for HOQ as was shown for SWQ. The only minor difference worth noting is that the HOQ case shows a less pronounced “thickening” of y^+ in region 2 ($-2 < z \leq 0$ mm). This feature is caused by the larger scatter in the measured gas temperature, which causes the less pronounced increase in viscosity at this location.

4.2.3 u_z^+, y^+ velocity profiles

The analysis proceeds with an evaluation of the non-dimensional boundary layer variables u_z^+, y^+ in relation to SWQ and HOQ flame topologies. This analysis is separated in terms of the fluid approaching the quenching location from $-2 \leq z \leq 0$ mm and the fluid immediately downstream the quenching location in the burned gas boundary layer from $0 \leq z \leq 2$ mm. Figure 7 shows these two regions relative to $z = 0$ mm for both SWQ and HOQ. The black-dotted and -dashed lines refer to the inner scaling velocity equations, namely Eq. 4 and 5 for the viscous sublayer (dotted) and the log-layer (dashed), respectively. Recall that the u_z^+, y^+ profiles for the non-reacting flow conform to the dashed- and dotted-lines for $y^+ < 8$ and from $20 \leq y^+ \leq 50$ (see Fig. 3b).

For both the SWQ and HOQ topologies, the reacting flow u_z^+ profiles follow the linear regime of the viscous sublayer up to $y^+ = 5$, indicating that the universal linear scaling law, $u^+ = y^+$, remains to be an accurate scaling law in the viscous sublayer, even at the quenching location. Beyond $y^+ > 5$, the u_z^+ profiles become sub-linear and deviate significantly from both scaling laws with u_z^+ being much smaller than that of the non-reacting flow. For SWQ topologies, a progression of the u_z^+ profiles towards lower values is evident as z progresses from -2 mm to 0 mm (i.e., as the flow approaches the quenching location). Downstream the quenching location, the u_z^+ values show a gradual progression towards larger values as z progresses from 0 mm to 2 mm. At $z = 2$ mm, u_z^+ profiles begin to approach the log-layer scaling depicted by the dashed-line, which may be a result of the developing burned gas boundary layer after quenching. For HOQ, u_z^+ profiles beyond $y^+ > 5$ also exhibit the strong deviation from the scaling laws with lower u_z^+ values, however, there is little discernible difference among u_z^+ profiles from $-2 \leq z \leq 0$. Downstream $z = 0$, the u_z^+ profiles exhibit

a slight increase in value, but the profiles at $z = 2$ mm still exhibit substantial deviation from the log-law scaling.

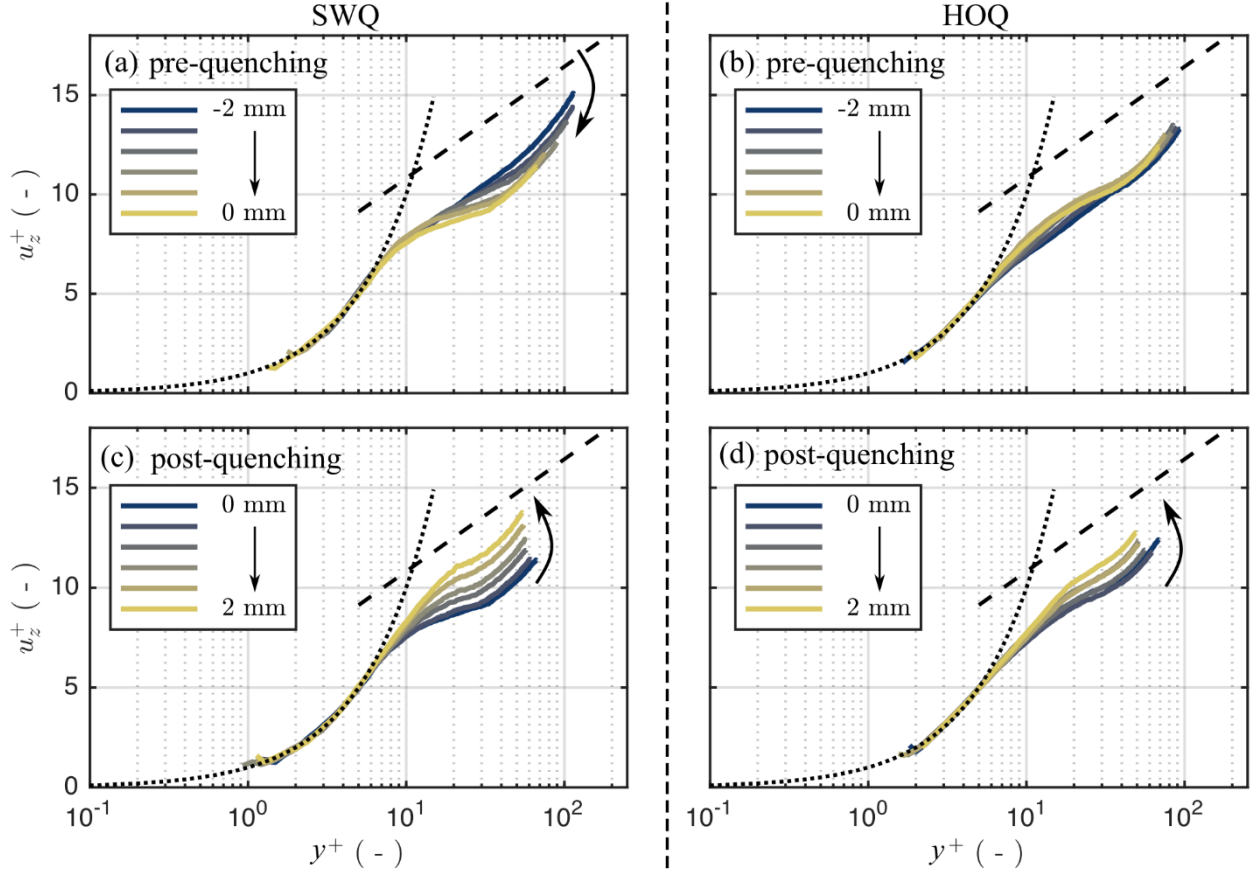


Fig. 7: Reacting turbulent boundary layer u_z^+, y^+ profiles. (a,c) SWQ cases, (b,d) HOQ cases. Statistical information: 868 samples for SWQ and 1132 samples for HOQ.

To understand the deviation in u_z^+ profiles of the reacting flow from that of the non-reacting flow, the variables that define u_z^+ (i.e. $\langle U_z \rangle$ and $u_{\tau,z}$) are evaluated in detail in Fig. 8. Figure 8 shows streamwise quantities of $\langle U_z \rangle$ within the viscous sublayer ($y^+ = 5$) and at various y^+ locations within the log-layer, as well as streamwise quantities of $u_{\tau,z}$. These streamwise velocity profiles are shown for the non-reacting flow, and both SWQ and HOQ flame topologies with emphasis on the $-2 \leq z \leq 2$ mm domain discussed in Fig. 7.

Figure 8 shows that each velocity profile for the non-reacting flow exhibits a relatively constant velocity in the streamwise direction. The $u_{\tau,z}$ profile for the non-reacting flow exhibits fluctuations around the mean value of 0.18; these fluctuations are primarily caused by fluctuations in the calculated velocity gradient at the wall $(d\langle U_z \rangle / dy)|_{y=0}$. The velocity profiles for the reacting flow, on the other hand, show a strong variation in the streamwise direction. In addition, the velocity values for the reacting flow are substantially larger than the non-reacting flow in all instances. As mentioned in Sect. 4.2.1, in addition to the flame imposing higher velocities as the flame approaches the wall, higher velocities for the reacting flow are a result of fluid expansion across the flame front, which accelerates the fluid across the flame front and entrains fresh gas into the flame. For the reacting flow, Fig. 8 shows that the profile shape of $\langle U_z \rangle$ in the viscous sublayer and $u_{\tau,z}$ emulate each other, although $u_{\tau,z}$ exhibits larger relative changes. $\langle U_z \rangle$ and $u_{\tau,z}$ show a considerable increase in velocity as the fluid approaches $z = 0$ mm, followed by decreasing velocities further downstream of $z = 0$ mm. The reacting velocity profiles for $y^+ = 30 - 50$ show a monotonically increasing velocity in the streamwise direction.

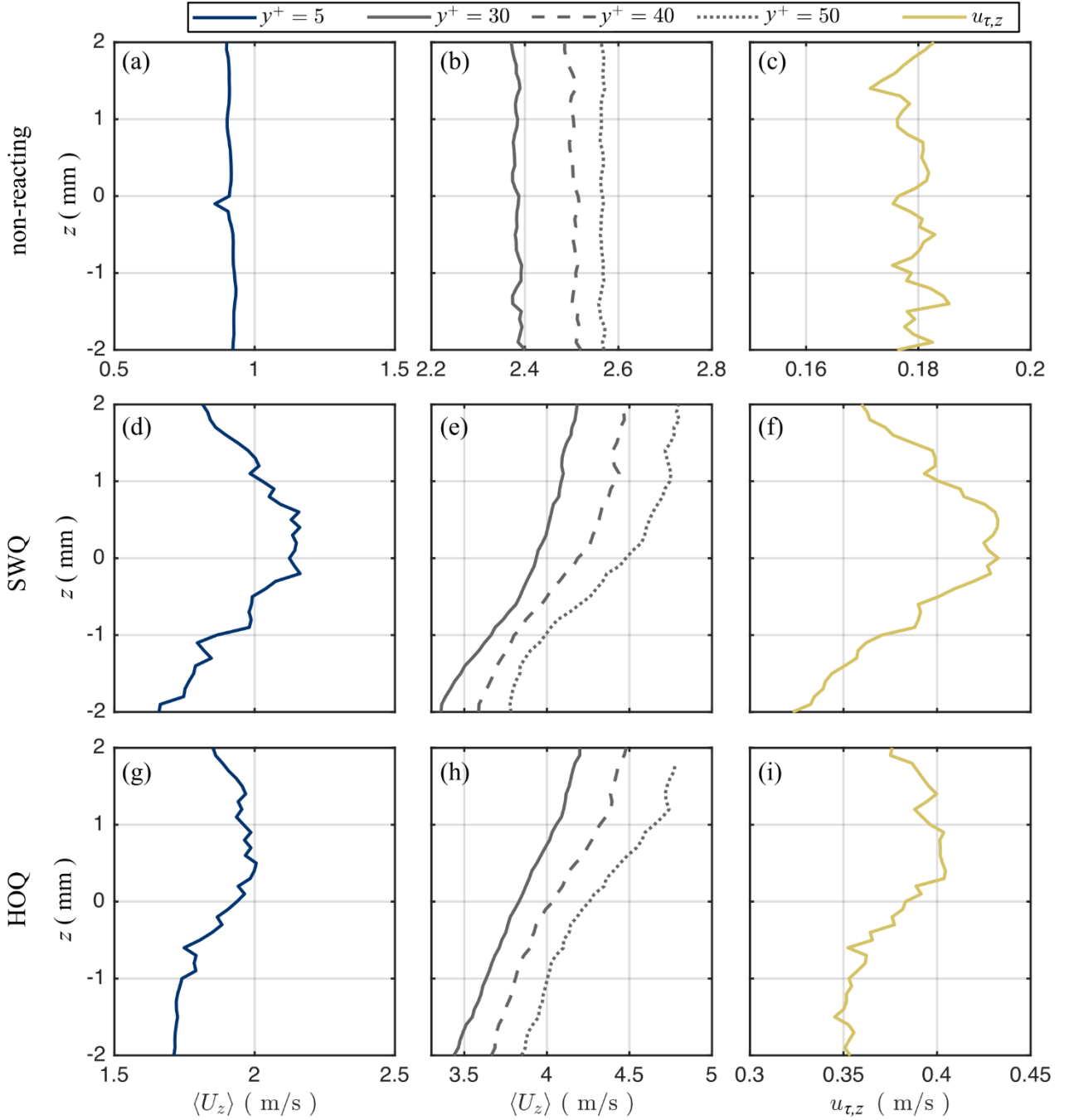


Fig. 8: Streamwise quantities of $\langle U_z \rangle$ and $u_{\tau,z}$ for non-reacting (a-c), SWQ cases (d-f) and HOQ cases (g-i). $\langle U_z \rangle$ quantities are shown in the viscous sublayer ($y^+ = 5$, (a,d,g)) and at various locations in the log-law layer ($y^+ = 30, 40, 50$ (b,e,h)).

To understand how the velocity differences between non-reacting and reacting conditions shown in Fig. 8 contribute to the “flattened” u_z^+ profiles deviating from the law-of-the wall, the relative difference in velocity between non-reacting and reacting conditions is evaluated as follows:

$$(u_{\text{reacting}} - u_{\text{non-reacting}}) / u_{\text{non-reacting}} \cdot 100\% \quad (7)$$

In Eq. 7, the variable u corresponds to $u_{\tau,z}$, $\langle U_z \rangle$, or u_z^+ . Figure 9a,c shows the relative differences of $u_{\tau,z}$ and $\langle U_z \rangle$ at the y^+ locations shown in Fig. 8. These differences are shown for discrete z -locations. Figure 9b,d reveals the relative difference of u_z^+ as a result of the relative differences between $u_{\tau,z}$ and $\langle U_z \rangle$.

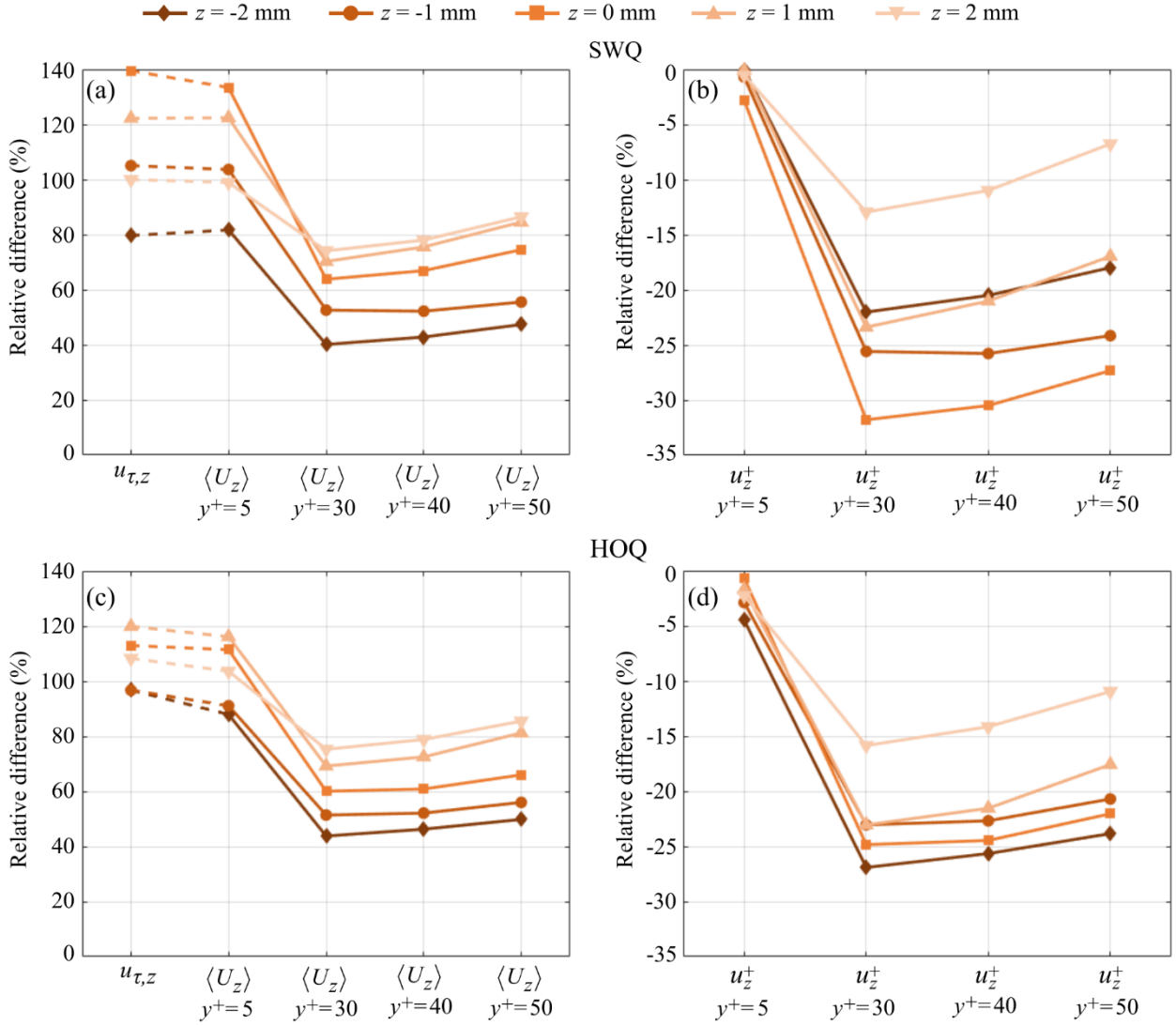


Fig. 9: Relative difference in $u_{\tau,z}$, $\langle U_z \rangle$, and u_z^+ between reacting and non-reacting values for (a,b) SWQ and (c,d) HOQ. The dotted lines between $u_{\tau,z}$ and $\langle U_z \rangle$ are used to help compare the value of these two variables.

Figure 9 reveals that both $u_{\tau,z}$ and $\langle U_z \rangle_{y^+=5}$ have the largest increase relative to the non-reacting flow. However, the amount of increase in these quantities is very similar, which is sensible since these parameters are expected to be governed by the same local velocity and fluid properties. The similarity between $u_{\tau,z}$ and $\langle U_z \rangle$ from the reacting and non-reacting cases is congruent for all regions within $y^+ \leq 5$. As a result, the SWQ and HOQ reacting boundary layers in the u_z^+, y^+ space show almost no deviation from the non-reacting boundary layer within the viscous sublayer. Each boundary layer adheres to the linear $u^+ = y^+$ scaling law, despite having significantly higher velocities and a flame present for the reacting cases. In the log-layer, the relative increase in $\langle U_z \rangle$ between reacting and non-reacting cases is less substantial than the relative increase in $u_{\tau,z}$. The larger increase in $u_{\tau,z}$ than $\langle U_z \rangle$ effectively reduces u_z^+ in the log-layer, causing the deviation of u_z^+ from the non-reacting case and from the law-of-the-wall.

The extent to which u_z^+ deviates from the law-of-the-wall is determined by the disparity between the relative difference of $u_{\tau,z}$ and $\langle U_z \rangle$ in the log-layer. Since the relative difference of $u_{\tau,z}$ is much larger than the relative difference in $\langle U_z \rangle$ in the log-layer, the following discussion focuses on the parameters contributing to changes in $u_{\tau,z}$; namely $d\langle U_z \rangle/dy|_{y=0 \text{ mm}}$ and ν , which are both proportional to $u_{\tau,z}$ and thus inversely proportional to u_z^+ .

When evaluating the velocity fields for the non-reacting and reacting flows in Figs. 3-6, it is clear that $d\langle U_z \rangle/dy|_{y=0}$ increases for the reacting boundary layer due to an increase in velocity at the wall. However, a more influential factor contributing to an increase in $u_{\tau,z}$ for the reacting flow is the near-wall gas temperature,

which governs ν . This aspect is admirably shown for the SWQ topology, where a distinct near-wall temperature gradient is resolved as a function of streamwise distance. Evaluating the profiles shown in Fig. 5, at $z = -2$ mm the gas temperature is shown to increase, while $d\langle U_z \rangle / dy$ at the wall reaches its peak. At this z -location, the increase in ν as well as $d\langle U_z \rangle / dy$ both contribute to the relative increase in $u_{\tau,z}$. However, from $-2 \leq z \leq 0$ mm, $u_{\tau,z}$ increases substantially, while $d\langle U_z \rangle / dy$ decreases. In these z -locations, the increase in $u_{\tau,z}$ is strongly driven by the increase in ν due to the sharp temperature rise near flame quenching. In turn, this increase in $u_{\tau,z}$ reduces u_z^+ , contributing to the “flattening” of the u_z^+ curves in Fig. 7a as z increases from -2 mm to 0 mm. Downstream of the $z = 0$ mm location, Fig. 5 shows that the near wall temperature (and ν) are relatively constant, while $d\langle U_z \rangle / dy$ at the wall decreases, thereby decreasing $u_{\tau,z}$. At the same time, $\langle U_z \rangle$ in the log-layer increases above $z = 0$ mm as shown in Fig. 8. The increase in $\langle U_z \rangle$ and decrease in $u_{\tau,z}$ increases u_z^+ , which describes the mild transition of u_z^+ back towards values of the non-reacting flow as shown in Fig. 7c. The relative deviations of $u_{\tau,z}$, $\langle U_z \rangle$, and u_z^+ from the non-reacting flow as a function of z -location in Fig. 9a,b accurately describe the changes of u_z^+ relative to one another in Fig. 7a,c.

The observation that the reacting flow u_z^+ profiles undershoot the log-law has also been reported by Alshaalan and Rutland [7], who numerically studied SWQ flame quenching. They attributed the reduction of u_z^+ to the stronger increase in $u_{\tau,z}$ compared to $\langle U_z \rangle$, but did not evaluate the effect of gas temperature and ν towards the increase in $u_{\tau,z}$. Similar to the results in this work, Alshaalan and Rutland also observed that u_z^+ return towards the universal log-law farther downstream of the flame quenching location [7].

For HOQ cases, Fig. 9c shows that the relative difference in $u_{\tau,z}$ is high, but the variation in $u_{\tau,z}$ at the various z -locations is less than SWQ cases. The high relative difference, but lower variation in $u_{\tau,z}$ is due to the higher viscosity already occurring at $z = -2$ mm and the milder streamwise gradient in viscosity as shown in Fig. 6b. The larger relative difference in $u_{\tau,z}$ compared to $\langle U_z \rangle$ in the log-layer reduces u_z^+ as shown in Fig. 9c,d and leads to the “flattening” of u_z^+ profiles shown in Fig. 7b,d. However, for HOQ, the variation in the relative difference of u_z^+ in the log-layer is smaller than for SWQ, and there does not appear to be a systematic increase/decrease as z increases from -2 mm to 1 mm (Fig. 9d). As such, the u_z^+ profiles shown in Figs. 7b,d are closely spaced and do not show a systematic progression as z increases from -2 mm to 1 mm. It is not until z increases from 1 mm to 2 mm when an increase in $\langle U_z \rangle$ in the log-layer (see Fig. 8) increases u_z^+ profiles in the direction towards the law-of-the-wall (see Fig. 7d).

This analysis reveals the unique aspects of FWI that fundamentally change the turbulent boundary layer, and suggests additional considerations beyond the traditional wall-models are required to accurately predict the boundary layer processes in FWI. The evolution of u_z^+ , y^+ in time and space features a complex interaction between the contributions of (1) thermal expansion by heat release, (2) flame topology at the wall, (3) near-wall temperature and fluid viscosity, and (4) near-wall velocity gradient. The thermal expansion induces higher velocities across the flame front, which increases $\langle U_z \rangle$ in the log-layer. In the viscous sublayer, the flame approaching the wall increases $\langle U_z \rangle$ at the wall. The flow in the viscous sublayer is further complicated when the flame drastically increases temperature and fluid viscosity, which is correlated with a decrease in $\langle U_z \rangle$ at the wall. Accurately measuring the gas temperature in between the flame and wall is challenging during FWI, which often feeds into the limited capability of developing more accurate numerical models. This work provides insight into the effects of gas phase temperature on the boundary layer behavior in attempt to foster opportunities to improve numerical modeling efforts.

5. Conclusions

This work studied the turbulent boundary layer evolution in the presence of FWI. Simultaneous PIV and OH-LIF was used to measure the velocity field and flame front distribution near the wall. A complementary experiment employing DP-CARS and OH-LIF was used to measure gas temperature and flame distribution under identical operating conditions to provide a reasonable measure of kinematic viscosity for proper normalization of u_z^+ , y^+ variables. Experiments were conducted in a SWQ burner, comprised of a V-flame impinging onto a temperature-controlled vertical stainless-steel wall. Measurements were conditionally sampled based on the flame topology (SWQ vs. HOQ), as well as the flame impingement height on the wall.

The non-dimensional boundary layer variables u_z^+, y^+ were calculated to evaluate the turbulent boundary layer structure. It was shown that regardless of the FWI topology, the reacting flow u_z^+ profiles follow the linear scaling law, $u^+ = y^+$ in the viscous sublayer up to $y^+ = 5$, revealing that this law is credible for FWI environments. Beyond $y^+ = 5$, the u_z^+ velocity becomes sublinear and deviates from the traditional law-of-the-wall scaling with u_z^+ being much smaller than that of the non-reacting flow in the log-layer. The flame modifies the near-wall velocity field as well as the temperature field, which are both responsible for the deviations in u_z^+ . Upstream the flame impingement location, the flame increases the fresh-gas streamwise velocity $\langle U_z \rangle$, as well as the near-wall velocity gradient $d\langle U_z \rangle/dy|_{y=0}$. As the fluid approaches the flame impingement location, the gas temperature increases strongly, causing a three-fold increase in the fluid's kinematic viscosity, ν . At this location, $\langle U_z \rangle$ and $d\langle U_z \rangle/dy|_{y=0}$ begin to decrease, presumably due to increased viscosity. The significant increase in ν increases $u_{\tau,z}$, which in turn decreases u_z^+ and contributes to the flattening of the u_z^+ profiles compared to the law-of-the-wall scaling. Downstream the flame impingement location, gas temperature and ν values stabilize, and a burned gas boundary layer develops. The high viscosity at the wall reduces $d\langle U_z \rangle/dy|_{y=0}$ in the burned gas boundary layer, while $\langle U_z \rangle$ increases away from the wall. The former reduces $u_{\tau,z}$, which in combination with higher $\langle U_z \rangle$ away from the wall, initiates an increase in u_z^+ with downstream distance from the flame impingement location, and the u_z^+ profiles begin to approach the law-of-the-wall scaling in the log-layer.

The said trends are most pronounced for SWQ cases reported in this work. For HOQ cases, a considerable scatter in the measured gas temperature produced a weaker perceived gas temperature gradient, for which the trends upstream of the flame impingement location were less pronounced. As such, HOQ findings should be taken with caution. Nonetheless, the work identifies the fluid mechanic and thermofluid property modifications imposed by FWI, which results in an appreciable deviation from traditional wall models. It is intended that such measurements can be used to help generate more appropriate wall models for FWI.

While the measurements are presented in non-dimensionalized form to aid generalization of the findings, it is important to emphasize that the findings may be specific to the operating conditions employed. The findings reported here are in agreement with DNS studies from Ashaalan and Rutland [7], which exhibited lower turbulence levels and incorporated fuel properties different to those presented here. Nonetheless, it would be valuable to investigate the effect of higher turbulence levels and various fuel properties to understand potential changes in the near-wall flame/flow processes and how such changes may affect the boundary layer behavior.

Acknowledgements

This project is funded by the Deutsche Forschungsgemeinschaft (DFG, German Research Foundation) Projektnummer 237267381 TRR 150. Robert S. Barlow is grateful for a related DFG Mercator Fellowship. The generous financial support is gratefully acknowledged. A. Dreizler is grateful for support through the Gottfried Wilhelm Leibniz program. B. Peterson gratefully acknowledges funding from the European Research Council (grant no. 759546) and Engineering Physical Science Research Council (EP/V003283/1).

Declaration of Competing Interest

The authors declare that they have no known competing financial interests or personal relationships that could have appeared to influence the work reported in this paper.

References

1. G. Borman, K. Nishiwaki, Internal-combustion engine heat transfer, *Prog. Energy Combust. Sci.* 13 (1987) 1-46.
2. A. Dreizler, B. Böhm, Advanced laser diagnostics for improved understanding of premixed flame-wall interactions, *Proc. Combust. Inst.* 35 (2015) 37-64.
3. A.Y. Alharbi, V. Sick, Investigation of boundary layers in internal combustion engines using a hybrid algorithm of high speed micro-PIV and PTV, *Exp. Fluids* 49 (2010) 949-959.
4. C. Jainski, L. Lu, A. Dreizler, V. Sick, High-speed micro particle image velocimetry studies of boundary-layer flows in a direct-injection engine, *Int. J. Engine Res.* 14 (2013) 247-259.
5. C.P. Ding, B. Peterson, M. Schmidt, A. Dreizler, B. Böhm, Flame/flow dynamics at the piston surface of an IC engine measured by high-speed PLIF and PTV, *Proc. Combust. Inst.* 37 (2019) 4973-4981.

6. P. Johe, F. Zentgraf, M. Greifenstein, M. Steinhausen, C. Hasse, A. Dreizler, Characterization of flow field and combustion dynamics in a novel pressurized side-wall quenching burner using high-speed PIV and OH-PLIF measurements, *Int. J. Heat Fluid Flow* 94 (2022) 108921.
7. T.M. Alshaalan, C.J. Rutland, Turbulence, scalar transport, and reaction rates in flame-wall interaction, *Symposium (International) on Combustion* 27 (1998) 793-799.
8. T.J. Poinso, D.C. Haworth, G. Bruneaux, Direct simulation and modeling of flame-wall interaction for premixed turbulent combustion, *Combust. Flame* 95 (1993) 118-132.
9. U. Ahmed, N. Chakraborty, M. Klein, Influence of flow configuration and thermal wall boundary conditions on turbulence during premixed flame-wall interaction within boundary layers, *Flow Turbul. Combust.* 111 (2023) 825-866.
10. A. Gruber, R. Sankaran, E.R. Hawkes, and J.H. Chen, Turbulent flame-wall interaction: a direct numerical simulation study, *J. Fluid Mech.* 658 (2010) 5-32.
11. H. Kosaka, F. Zentgraf, A. Scholtissek, C. Hasse, A. Dreizler, Effect of flame-wall interaction on local heat release of methane and DME combustion in a side-wall quenching geometry, *Flow Turbul. Combust.* 104 (2020) 1029-1046.
12. T. Alshaalan, C.J. Rutland, Wall heat flux in turbulent premixed reacting flow, *Combust. Sci. Technol.* 174 (2002) 135-165.
13. A.O. Ojo, D. Escofet-Martin, J. Collins, G. Falconetti, B. Peterson, Experimental investigation of thermal boundary layers and associated heat loss for engine relevant processes using HRCARS and phosphor thermometry, *Combust. Flame* 233 (2021) 111567.
14. S.Kr. Ghai, U. Ahmed, N. Chakraborty, Effects of fuel Lewis number on wall heat transfer during oblique flame-wall interaction of premixed flames within turbulent boundary layers, *Flow Turbul. Combust.* 111 (2023) 867-895.
15. A.O. Ojo, D. Escofet-Martin, B. Peterson, High-precision 2D phosphor thermometry at kHz-rates during flame-wall interaction in narrow passages, *Proc. Combust. Inst.* 39 (2023) 1455-1463.
16. T.J. Poinso, D.C. Haworth, G. Bruneaux, Direct simulation and modeling of flame-wall interaction for premixed turbulent combustion, *Combust. Flame* 95 (1993) 118-132.
17. A. Heinrich, F. Ries, G. Kuenne, S. Ganter, C. Hasse, A. Sadiki, and J. Janicka, „Large eddy simulation with tabulated chemistry of an experimental sidewall quenching burner,” *Int. J. Heat Fluid Flow* 71, 95-110 (2018).
18. T. Zirwes, T. Häber, F. Zhang, H. Kosaka, A. Dreizler, M. Steinhausen, C. Hasse, A. Stagni, D. Trimis, R. Suntz, and H. Bockhorn, „Numerical study of quenching distances for side-wall quenching using detailed diffusion and chemistry,” *Flow Turbul. Combust.* 106, 649-679 (2021).
19. A.O. Ojo, D. Escofet-Martin, C. Abram, B. Fond, B. Peterson, Precise surface temperature measurements at kHz-rates using phosphor thermometry to study flame-wall interactions in narrow passages, *Combust. Flame* 240 (2022) 111984.
20. H. Kosaka, F. Zentgraf, A. Scholtissek, L. Bischoff, T. Häber, R. Suntz, B. Albert, C. Hasse, A. Dreizler, Wall heat fluxes and CO formation/oxidation during laminar and turbulent side-wall quenching of methane and DME flames, *Int. J. Heat Fluid Flow* 70 (2018) 181-192.
21. F. Zentgraf, P. Johe, M. Steinhausen, C. Hasse, M. Greifenstein, A.D. Cutler, R.S. Barlow, A. Dreizler, Detailed assessment of the thermochemistry in a side-wall quenching burner by simultaneous quantitative measurement of CO₂, CO and temperature using laser diagnostics, *Combust. Flame* 235 (2021) 111707.
22. F. Zentgraf, P. Johe, A.D. Cutler, R.S. Barlow, B. Böhm, A. Dreizler, Classification of flame prehistory and quenching topology in a side-wall quenching burner at low-intensity turbulence by correlating transport effects with CO₂, CO and temperature, *Combust. Flame* 239 (2022) 111681.
23. M. Steinhausen, T. Zirwes, F. Ferraro, A. Scholtissek, H. Bockhorn, C. Hasse, Flame-vortex interaction during turbulent side-wall quenching and its implications for flamelet models, *Proc. Combust. Inst.* 39 (2023) 2149-2158.
24. C. Jainski, M. Reißmann, S. Jakirlic, B. Böhm, and A. Dreizler, “Quenching of premixed flames at cold walls: effects on the local flow,” *Flow Turbul. Combust.* 100, 177-196 (2018).
25. C. Jainski, M. Reißmann, B. Böhm, A. Dreizler, Experimental investigation of flame surface density and mean reaction rate during flame-wall interaction, *Proc. Combust. Inst.* 36 (2017) 1827-1834.
26. G. Bruneaux, T. Poinso, J.H. Ferziger, Premixed flame-wall interaction in a turbulent channel flow: budget for the flame surface density evolution equation and modelling, *J. Fluid Mech.* 349 (1997) 191-219.
27. U. Ahmed, N. Chakraborty, M. Klein, Scalar gradient and strain rate statistics in oblique premixed flame-wall interaction within turbulent channel flows, *Flow Turbul. Combust.* 106 (2021) 701-732.
28. U. Ahmed, N. Chakraborty, and M. Klein, Assessment of Bray Moss Libby formulation for premixed flame-wall interaction within turbulent boundary layers: influence of flow configuration, *Combust. Flame* 233 (2021) 111575.

29. U. Ahmed, N. Chakraborty, M. Klein, Influence of thermal wall boundary conditions on scalar statistics during flame-wall interaction of premixed combustion in turbulent boundary layers, *Int. J. Heat Fluid Flow* 92 (2021) 108881.
30. P. Johe, F. Zentgraf, M. Greifstein, R.S. Barlow, A. Dreizler, Laser-based investigation of flame surface density and mean reaction rate during flame-wall interaction at elevated pressure, *Proc. Combust. Inst.* 39 (2023) 2159-2168.
31. H. Schlichting, K. Gerstein, *Boundary-layer theory*, Springer, Berlin, Heidelberg, 10th Edition, 2006.
32. S. B. Pope, *Turbulent Flows*, Cambridge University Press, Cambridge, 2000.
33. M. Schmidt, C.-P. Ding, B. Peterson, A. Dreizler, B. Böhm, Near-wall and flame and flow measurements in an optically accessible SI engine, *Flow Turbul. Combust.* 106 (2021) 597-611.
34. F. Zentgraf, Investigation of reaction and transport phenomena during flame-wall interaction using laser diagnostics, PhD Dissertation, Technical University of Darmstadt (2022) <https://doi.org/10.26083/tuprints-00021314>.
35. A. Renaud, C.-P. Ding, S. Jakirlic, A. Dreizler, B. Böhm, Experimental characterization of the velocity boundary layer in a motored IC engine, *Int. J. Heat Fluid Flow* 71 (2018) 366-377.
36. A. Sciacchitano, B. Wieneke, PIV uncertainty propagation, *Meas. Sci. Technol.* 27 (2016) 084006.
37. B. Wieneke, Fundamentals of digital particle image velocimetry, *Meas. Sci. Technol.* 13 (1997) 1379-1392.
38. H. Hill, C.-P. Ding, E. Baum, B. Böhm, A. Dreizler, B. Peterson, An application of tomographic PIV to investigate the spray-induced turbulence in a direct-injection engine, *Int. J. Multiphase Flow* 121 (2019) 103116.
39. R. P. Lucht, V. Velur-Natarajan, C.D. Carter, K.D. Grinstead Jr, J.R. Gord, P.M. Danehy, G.J. Fiechtner, R.L. Farrow, Dual-pump coherent anti-Stokes Raman scattering temperature and CO₂ concentration measurements, *AIAA Journal* 41 (2003) 679-686.
40. A.D. Cutler, E.C.A. Gallo, L.M.L. Cantu, WIDECARS spectra fitting in a premixed ethylene-air flame, *J. Raman Spectroscopy* 47 (2016) 416-424.
41. Y. A. Çengel, J. M. Cimbala, *Fluid Mechanics: Fundamentals and Applications*, McGraw-Hill, New York, NY, 3rd edition, 2014.
42. A. Nicolas, F. Zentgraf, M. Linne, A. Dreizler, B. Peterson Assessment and application of wavelet-based optical flow velocimetry (wOFV) to wall-bounded turbulent flows, *Exp. Fluids* 60 (2023) 50.
43. B. Boust, J. Sotton, S.A. Labuda, M. Bellenoue, A thermal formulation for single-wall quenching of transient laminar flames, *Combust. Flame* 149 (2007), 286-294.
44. D. Escofet-Martin, A.O. Ojo, N.T. Mecker, M.A. Linne, B. Peterson, Simultaneous 1D hybrid fs/ps rotational CARS, phosphor thermometry, and CH* imaging to study transient near-wall heat transfer processes, *Proc. Combust. Inst.* 38 (2021) 1579-1587.
45. A. Bohlin, C. Jainski, B.D. Patterson, A. Dreizler, C.J. Kliewer, Multiparameter spatio-thermochemical probing of flame-wall interactions advanced with coherent Raman imaging, *Proc. Combust. Inst.* 36 (2017) 4557-4564.